Dalton Transactions

ROYAL SOCIETY OF CHEMISTRY

PAPER

View Article Online
View Journal | View Issue

Cite this: *Dalton Trans.*, 2026, **55**, 2485

Bio-reductive hetero-bimetallic Co(III)–Pt(II) complex for tumor-selective platinum release and cytotoxicity

Sharmila Wahengbam,[a] Neha Masarkar,[b] Himanshi Sharma,[c] Sukhes Mukherjee,[b] Chandi C. Malakar [a] and Mithun Roy *[d]

The application of bioreductive metalloprodrugs in cancer therapy has emerged as a promising strategy to achieve site-specific activation of cytotoxic agents by exploiting the reductive microenvironment which is a characteristic of tumors, thereby minimizing off-target effects. In this study, we report the synthesis of a heterobimetallic **[Co(III)–Pt(II)]** complex designed to harness the tumor-specific redox conditions for selective anticancer activity. The complex was thoroughly characterized using a suite of spectroscopic techniques, and its redox behavior was investigated *via* electrochemical analysis, which revealed a quasi-reversible one-electron reduction with an $E_{1/2}$ value of −0.52 V *vs.* Ag/AgCl—suggesting the feasible reduction of Co(III) under biologically relevant conditions. Cellular uptake studies, performed using inductively coupled plasma mass spectrometry (ICP-MS), demonstrated efficient internalization of the complex within 12 hours in A549 lung carcinoma cells. Furthermore, binding studies with 5′-guanosine monophosphate (5′-GMP), conducted *via* electrospray ionization mass spectrometry (ESI-MS), confirmed the reductive release of the Pt(II) fragment and its subsequent coordination with nucleophilic targets. Induction of apoptosis was verified using Annexin V assays, indicating the activation of programmed cell death pathways. The complex exhibited potent cytotoxicity under both normoxic and hypoxic conditions in A549 cells and showed significant activity against a panel of cancer cell lines, including HT-29 (colorectal), MCF-7 (breast), and MDA-MB-231, a highly aggressive triple-negative breast cancer line. These findings highlight the potential of this redox-responsive bimetallic complex as a next-generation anticancer agent capable of overcoming platinum resistance, enhancing tumor selectivity, and reducing systemic toxicity relative to conventional platinum-based therapies.

Received 25th September 2025,
Accepted 19th January 2026

DOI: 10.1039/d5dt02296g

rsc.li/dalton

Introduction

The therapeutic success achieved through molecular targeted therapies, immunotherapies, and chemotherapy has a profound impact on the evolution of modern medicine.[1–5] Despite significant advances, chemotherapy remains a cornerstone in the treatment of solid tumors and late-stage cancers.[6,7] Among the chemotherapeutic agents, platinum-based complexes, including cisplatin, carboplatin, and oxaliplatin, have served as a mainstay in the treatment of various malignancies since the 1970s, owing to their potent cytotoxic effects and broad-spectrum activity.[8–12] Their primary mechanism of action involves the formation of crosslinks with the guanine residue of DNA, thereby interfering with replication and transcription, ultimately leading to cell death.[13–15] However, the clinical potential of these platinum-based drugs is significantly hindered by dose-limiting toxicity, such as nephrotoxicity and neurotoxicity, which contribute to severe systemic side effects.[16–20] Furthermore, these compounds often exhibit poor tumor selectivity, leading to off-target activation and reduced therapeutic indices. A particularly challenging issue is the rapid deactivation of Pt(II) by thiol-containing molecules, such as glutathione (GSH) and metallothionein (MT), which promotes the development of drug resistance.[21–23] Notably, the intracellular level of GSH is often several-fold higher in hypoxic cancer cells compared to normal cells.[24] Interestingly, this characteristic has now been harnessed to design prodrugs that remain stable in systemic circulation but are selectively activated within the reductive environment of tumor cells.[25–28] Besides the large number of organic prodrugs and various

[a]*Department of Chemistry, National Institute of Technology Manipur, Langol, Imphal West – 795004, India. E-mail: mithunroy@nita.ac.in, mithunroy.iisc@gmail.com*
[b]*Department of Biochemistry, All India Institute of Medical Sciences, Bhopal Saket Nagar, Bhopal, Madhya Pradesh – 462020, India. E-mail: sukhes.biochemistry@aiimsbhopal.edu.in*
[c]*Kusuma School of Biological Sciences, Indian Institute of Technology Delhi, Hauz Khas, New Delhi – 110016, India*
[d]*Department of Chemistry, National Institute of Technology Agartala, Jirania-799046, West Tripura, Tripura, India*

metal-based complexes, including Pt(IV), Ru(III), and Co(III) have been investigated as bio-reductive prodrugs that undergo activation *via* intracellular reductants, enabling site-specific release of cytotoxic agents in the tumor.[29–33] Among these, Pt(IV) complexes have been widely studied; however, they often demand relatively high reduction potentials and are prone to competing reduction pathways, leading to uncontrolled formation of active Pt(II) species.

This not only risks premature activation in acidic environments but can also trigger off-target DNA binding, causing toxicities similar to those of Pt(II) drugs.[34,35] Ru(III) complexes, while redox-active, generally possess slow ligand exchange kinetics, which may limit their therapeutic efficiency. They also show variable stability and sometimes fail to be selectively activated in hypoxic tumors. Additionally, their absorption, distribution, and elimination from the body are not yet fully understood, which can make their side effects unpredictable.[36,37a] In contrast, Co(III)-based complexes present several advantages. They feature more accessible redox potentials and undergo more favourable ligand exchange upon reduction. Replacement of O-donor ligand which typically stabilize the +2-oxidation state of cobalt with stronger N-donor ligand enhances the stability of the +3 oxidation state. This substitution consequently lowers the ε^0 value, as demonstrated in the studies of Hambley and co-workers.[37b,c] Moreover, cobalt(III) ions are relatively inert in oxygen-rich environments, allowing cobalt-based prodrugs to remain stable in the bloodstream until they reach the hypoxic tumor site, where they are reduced to the more reactive Co(II) state, releasing the active drug. Additionally, cobalt's biological relevance, as exemplified by its role in vitamin B_{12}, enhances its biocompatibility, making Co(III) a promising scaffold for bio-reductive prodrug development.[38,39] Expanding on these approaches, a growing number of bimetallic complexes have been engineered to leverage synergistic redox behaviours. For instance, Pt(IV)–Ru(II) systems utilize the Ru(II) centre to mediate electron transfer to the Pt(IV) moiety under reductive conditions, thereby promoting the controlled release of Pt(II).[40–42] Other bimetallic constructs, such as Rh(III)–Pt(II), **Co(III)–Ru(II)**, and Ir(III)–Pt(IV) complexes, have also been investigated to enhance the selectivity and efficacy of platinum-based chemotherapeutics.[43–45]

In this study, we engineered a hetero-bimetallic **Co(III)–Pt(II)** complex to exploit the redox imbalance characteristic of hypoxic tumor cells. The Co(III) centre, which is kinetically inert under physiological conditions, undergoes reduction to Co(II) in the presence of intracellular reducing agents such as glutathione (GSH). This reduction event triggers the activation or increased accessibility of the Pt(II) pharmacophore. The liberated Pt(II) species can subsequently coordinate with nucleophilic targets such as DNA bases. While GSH is traditionally known to deactivate Pt(II) species, in the present system, it functions primarily as a reductant, initiating the reduction of the Co(III) centre. This redox-responsive bimetallic complex thus offers a promising strategy to address key limitations of conventional mononuclear platinum-based chemotherapeutics, potentially enhancing tumor selectivity while minimizing off-target toxicity (Scheme 1). Herein, we report the synthesis and characterization of a hetero-bimetallic **[Co(III)–Pt(II)]** complex, along with its electrochemical behaviour, glutathione (GSH)-mediated reductive release of the Pt(II) pharmacophore, cytotoxicity evaluation against a broad spectrum of cancer cell lines, and a comprehensive investigation of its cell death mechanism. This study highlights the potential of the complex as a next-generation bio-reductive prodrug for targeted cancer therapy.

Results and discussion

Synthesis, characterization, and general aspects

A tetradentate Schiff-base ligand, *N*,*N*-(ethane-1,2-diyl)bis(1-(pyridine-2-yl)methanimine) (L^1), was synthesized following the procedure outlined in the literature and characterized before complexation.[46] The cobalt(III) complex, **[Co(III)(L^1)(phen-NH_2)](acac)$_3$**, where acac = acetylacetonato was obtained by mixing a methanolic solution of L^1 with the methanolic solution of tris(acetylacetonato)cobalt(III) [Co(acac)$_3$], and subsequent addition of L^2 (1,10-phenanthrolin-5-amine). The red polycrystalline solid of the complex, **[Co(III)(L^1)(phen-NH_2)](acac)$_3$** was obtained on slow evaporation of the resulting reaction mixture. The platinum(II) complex, **[Pt(II)(DABA)Cl_2]** ([Pt]) (DABA: 3,4-diaminobenzoic acid), was synthesized according to the previously published protocol.[47] The heterobimetallic **Co(III)–Pt(II)** complex, **[Co(III)–Pt(II)]** was synthesized according to the previously published protocol.[47]

The heterobimetallic **Co(III)–Pt(II)** complex, **[Co(III)–Pt(II)]** was synthesized by coupling **[Co(III)(L^1)(phen-NH_2)](acac)$_3$** and **[Pt(II)(DABA)Cl_2]** in methanol by EDC coupling method. Slow evaporation of the reaction mixture resulted in a red polycrystalline complex of **[Co(III)–Pt(II)]** (Scheme 2). All syn-

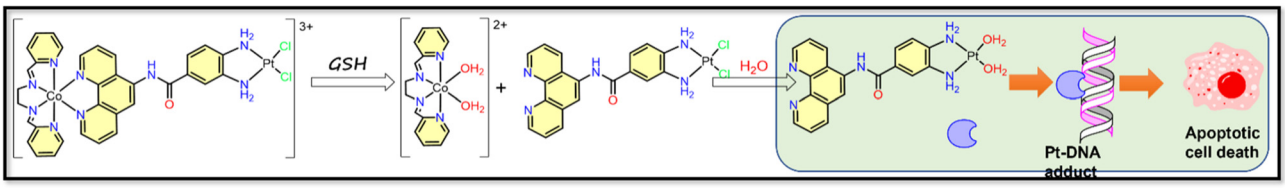

Scheme 1 Schematic representation of proposed hypothesis on GSH-assisted reductive elimination of Pt(II)-complex from **[Co(III)–Pt(II)]**, DNA-binding, and apoptotic cell death.

thesized complexes were characterized using a wide range of analytical and spectroscopic techniques, including UV-Visible spectroscopy, FT-IR spectroscopy, Q-TOF-ESI mass spectrometry, and proton nuclear magnetic resonance (^{1}H NMR) spectroscopy, confirming their structural and compositional properties. (Fig. S1–S10). The UV-visible spectra of **[Co(III)(L^1)(phen-NH$_2$)](acac)$_3$** recorded in 2% DMSO–PBS buffer (pH = 7.2) exhibited three characteristic bands, with a strong band at 264 nm attributed to π–π* transitions, an absorption band at 300 nm corresponding to a ligand to metal charge transfer (LMCT) transition, and another 444 nm assigned to d–d transition.[48] The FT-IR spectra of **[Co(III)(L^1)(phen-NH$_2$)](acac)$_3$** in the solid state exhibited a sharp peak at 1650 cm^{-1} (C=N$_{str}$), and a broad band at 3130 cm^{-1} for (N–H$_{str}$). The molar conductance (Λ_M) of the complex was found to be 186 S cm^2 mol^{-1}, indicating a 1 : 3 electrolytic nature with moderate dissociation in dimethyl formamide (DMF). The Q-TOF-ESI mass spectrum of the complex in methanol showed a molecular ion peak *m*/*z* at 164.0366 corresponding to the species [M]$^{3+}$. The complex, **[Co(III)(L^1)(phen-NH$_2$)](acac)$_3$** was also characterized using ^{1}H NMR (400 MHz, DMSO-d$_6$) spectra.

The UV-visible spectra of **[Pt(II)(DABA)Cl$_2$]** were characterized by a metal-to-ligand charge transfer (MLCT) transition at 712 nm in addition to the ligand-centered, π–π* and n–π* electronic transitions at 314 nm and 278 nm, respectively.[49a] Solid-phase FT-IR spectra of the complex, **[Pt(II)(DABA)Cl$_2$]**, typically demonstrated peaks at 1710–1720 cm^{-1} (O–H$_{str}$ of COOH group), 3439–2929 cm^{-1} (N–H$_{str}$, C–N$_{str}$, and O–H$_{str}$). The molar conductance (Λ_M) of the complex in dimethyl formamide (DMF) was found to be 15 S cm^2 mol^{-1}, suggesting a non-electrolytic nature of the complex. The molecular ion peak of *m*/*z* at 380.9736 corresponds to the species [M − Cl − H]$^+$ in the Q-TOF-ESI mass spectrum of the complex, **[Pt(II)(DABA)Cl$_2$]** in methanol. The complex, **[Pt(II)(DABA)Cl$_2$]**, was also further characterized with ^{1}H NMR (400 MHz, DMSO-d$_6$) spectra.

The UV-visible spectrum of **[Co(III)–Pt(II)]** recorded in 2% DMSO–PBS buffer (pH = 7.2) displayed three significant bands at around 723 nm, which was assigned to be d–π* transition (MLCT), the absorption at 445 nm corresponded to d–d transition, and other absorption bands at around 307 nm, 278 nm corresponding to the LMCT and π–π* transition. The complex displayed a typical FT-IR peak at 1656 cm^{-1} (C=N$_{str}$), 1669 cm^{-1} (C=O$_{str}$ of amide bond), and 3130 cm^{-1} (N–H$_{str}$). The molar conductance (Λ_M) of the complex was found to be 167 S cm^2 mol^{-1}, consistent with 1 : 3 electrolytic with moderate dissociation in dimethyl formamide (DMF). Q-TOF-ESI mass spectrum of the complex in methanol showed a molecular ion peak *m*/*z* at 297.1471 corresponding to the species [M]$^{3+}$, and the compound is also characterized using the ^{1}H NMR (400 MHz, DMSO-d$_6$) spectra.

Solubility and stability

The solubility of the complexes, namely **[Co(III)(L^1)(phen-NH$_2$)](acac)$_3$**, **[Pt(II)(DABA)Cl$_2$]**, and **[Co(III)–Pt(II)]** was probed across various solvents, including dimethylsulfoxide (DMSO), dimethylformamide (DMF), methanol, and acetonitrile where they demonstrated good to moderate solubility. Furthermore, the complexes were soluble in biologically relevant media, such as aqueous 2% DMSO solution in phosphate-buffered

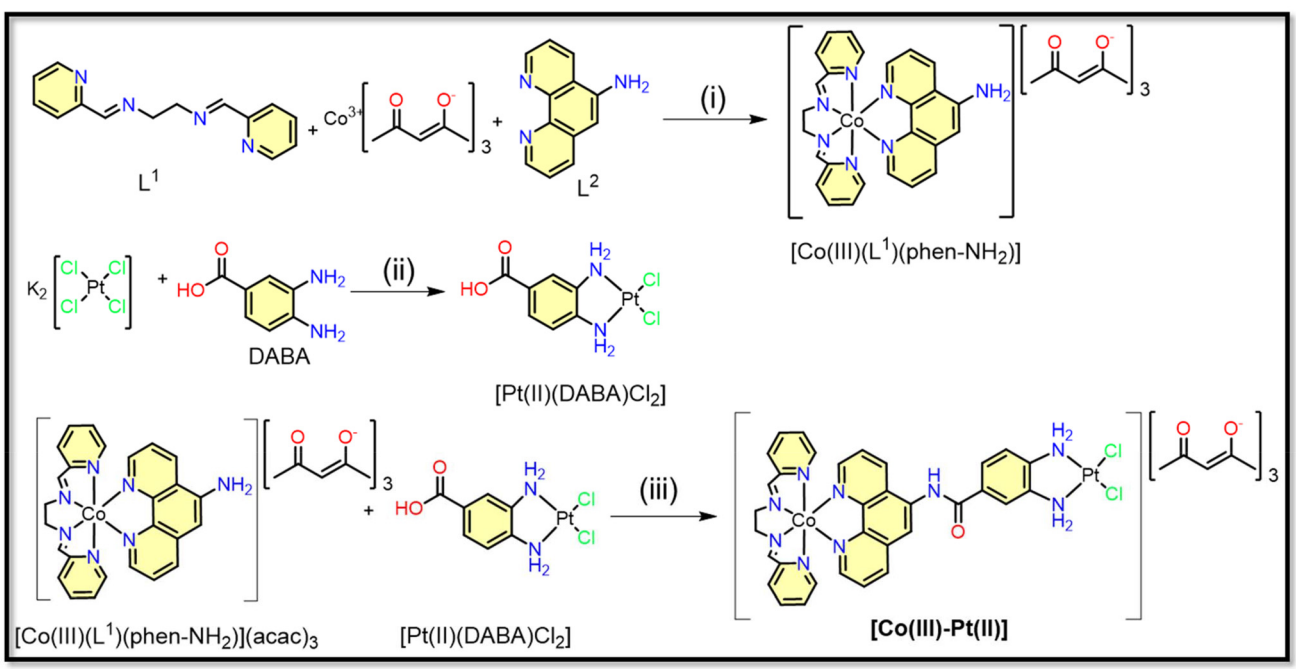

Scheme 2 Synthesis scheme for the complexes, **[Co(III)(L^1)(phen-NH$_2$)](acac)$_3$**, **[Pt(II)(DABA)Cl$_2$]** and **[Co(III)–Pt(II)]** complex. (i) CH_3OH, reflux, 6 h; (ii) DMF, RT, 8 h; (iii) DMF, 1-hydroxybenzotriazole (HOBt), 1-(3-dimethylaminopropyl)-3-ethylcarbodiimide hydrochloride (EDC·HCl), 12 h, RT.

saline (PBS, pH 7.2) buffer. However, their solubility was significantly limited in nonpolar solvents, such as hexane. Evaluating the stability of the complexes in physicochemical conditions is crucial for their potential use *in vitro* applications. Accordingly, stability studies of **[Co(III)–Pt(II)]** were conducted using a 2% DMSO–PBS buffer solution for 24 hours. Minimal variations in the UV-visible spectra were observed during this period, confirming that the complex remained stable in aqueous environments (Fig. S11). However, after an extended period, while the absorbance remains unchanged, the complex exhibited visible turbidity in aqueous solution, suggesting the onset of micro-aggregation rather than actual precipitation. Additionally, these compounds remained stable in the solid state for up to six months when stored at 0–4 °C in the dark. All biological assessments were performed using 2% DMSO–PBS buffer, with electronic spectroscopy employed for monitoring purposes.

Lipophilicity

Lipophilicity is an important parameter in drug development. It influences the adsorption of the complex, its distribution, and interaction with the biological membrane. It serves as an indicator of membrane permeability and bioavailability, which are essential for evaluating the potential of a compound as a therapeutic agent. The most commonly used method for determining lipophilicity is the shake flask method, which provides the partition coefficient (log *P* values) of a compound between an organic phase (*n*-octanol) and an aqueous phase (water). The log *P* values of the three metal complexes **[Co(III)(L^1)(phen-NH_2)](acac)$_3$**, **[Pt(II)(DABA)Cl_2]**, **[Co(III)–Pt(II)]** were determined using 2% DMSO–H_2O with *n*-octanol. The partition coefficient *P* was calculated as the ratio of a compound's concentration in the organic phase (octanol) to that in the aqueous phase. The average log *P* value obtained were 0.94 for **[Co(III)(L^1)(phen-NH_2)](acac)$_3$**, −0.34 for **[Pt(II)(DABA)Cl_2]**, and 1.15 for **[Co(III)–Pt(II)](acac)$_3$**. These values reflect varying degrees of lipophilicity, with **[Co(III)–Pt(II)]** having the highest affinity for the lipid phase, suggesting greater membrane permeability. The comparative lower log *P* value of **[Pt(II)(DABA)Cl_2]** arises from deprotonation of the free carboxylic acid group of the DABA ligand at physiological pH, which renders the complex anionic and reduces its distribution into the lipophilic octanol phase.[49b]

Electrochemical studies

The electrochemical behaviour of **[Co(III)(L^1)(phen-NH_2)](acac)$_3$**, **[Pt(II)(DABA)Cl_2]**, and the heterobimetallic **[Co(III)–Pt(II)]** complexes was investigated using cyclic voltammetry and differential pulse voltammetry. All the measurements were carried out with a glassy carbon working electrode, a platinum wire counter electrode, 0.1 M KCl as a supporting electrolyte, and an Ag/AgCl reference electrode at a scan rate of 50 mV s^{-1} (Fig. S12–S14). In the cathodic scan, both **[Co(III)(L^1)(phen-NH_2)](acac)$_3$** and **[Co(III)–Pt(II)]** exhibited quasi-reversible one-electron reduction processes, with $E_{1/2}$ values of −0.53 V and −0.525 V, respectively. These redox events are attributed to the reduction of Co(III) to Co(II).[50] Other ligand-centered oxidation peaks were observed at around 1.01 V and in the range 1.4–1.5 V for both complexes. The close similarity in $E_{1/2}$ values between the two Co(III) complexes indicated that the cobalt centre predominantly governed the redox activity, while the coordinating ligands might have a subtle influence on the electron transfer kinetics and redox potential without altering the fundamental redox mechanism. However, the cyclic voltammogram of **[Pt(II)(DABA)Cl_2]** showed an irreversible electron transfer process with an $E_{1/2}$ value of −0.655 V, likely due to slow electron transfer kinetics and limited redox reversibility.[51]

Further electrochemical characterisation of the **[Co(III)–Pt(II)]** complex was performed through successive cyclic voltammetry scans using a saturated calomel electrode (SCE) as the reference. Preliminary electrochemical studies were performed using an Ag/AgCl electrode, and were later repeated with an SCE to validate the reliability of the data. Successive scans over time showed minimal shift in peak potentials and negligible changes in current intensity, indicating that the complex maintained electrochemical stability and that the voltammetric response was reproducible under the experimental conditions (Fig. S15). Furthermore, a scan rate-dependent study of **[Co(III)–Pt(II)]** complex revealed that the cathodic peak current increased linearly with the square root of the scan rate ($V^{1/2}$), yielding a strong linear correlation value (R^2 = 0.986) (Fig. S16 and S17). This confirmed that the redox process was diffusion-controlled, which was in agreement with the Randles–Sevcik equation.[52]

BSA binding studies

Bovine Serum Albumin (BSA) binding studies are widely used in evaluating metal-based drug candidates, as BSA shares significant structural and homology with Human Serum Albumin (HSA), the primary protein responsible for transporting drugs in the bloodstream. To gain insights into how protein binding may influence the *in vivo* distribution, pharmacokinetics, and bioavailability of the **[Co(III)–Pt(II)]** complex, a systematic BSA binding study was conducted. BSA serves as an effective model for studying non-covalent interactions, including hydrophobic forces and hydrogen bonding at specific binding domains. It contains aromatic amino acid residues-tryptophan, tyrosine, and phenylalanine that contribute to its intrinsic fluorescence, making it an ideal probe for studying drug–protein interactions.[53]

Fluorescence emission measurements were performed using a HITACHI F-7000 spectrophotometer at 298 K, with excitation at 280 nm and emission monitored at 339 nm. Titration of BSA (3×10^{-5} M) with increasing concentrations of **[Co(III)–Pt(II)]** (0.4 mM) in a 10 mM Tris-HCl buffer (pH 7.2) resulted in a notable decrease in fluorescence intensity, indicating effective quenching upon complex addition. Quantitative analysis using Stern–Volmer and Scatchard plots yielded a binding constant of 1.71×10^5 M^{-1}, and the corresponding Gibbs free energy change (ΔG) was calculated to be −7.133 kcal mol^{-1}, signifying that the binding was both spontaneous and thermodynamically favourable under physiological conditions

(Fig. S18 and S19). Molecular Docking study revealed a binding affinity of −9.24 kcal mol^{-1}, which is in reasonable agreement with the experimental binding constant value. The interaction map revealed that the ligand is stabilized through hydrogen bonding with the aspartic acid residues, π-alkyl interaction with HIS-9, and π–σ interaction with LEU282. Collectively, these observation highlights that the binding affinity of the complex is primarily driven by electrostatic interactions, hydrogen bonding, and aromatic π-interactions, thereby supporting its potential for effective transport and distribution in biological systems.

GSH-mediated release of platinum

Tumour cells have a distinctive biochemical microenvironment characterized by elevated levels of intracellular antioxidants, particularly glutathione (GSH), which plays a pivotal role in maintaining redox homeostasis and protecting cells from oxidative stress.[54] This elevated GSH concentration serves as a potential biochemical trigger for activation of redox-sensitive metal-based prodrugs, enabling site-specific release of cytotoxic agents in tumour cells. The redox exchange between GSH and **[Co(III)–Pt(II)]** complex was systematically investigated using UV-visible absorption spectroscopy and electrochemical methods to examine electronic and structural changes upon interaction with GSH (Fig. 1).

The complex exhibits a prominent metal-to-ligand charge transfer (MLCT) absorption band around 710 nm. Notably, this absorption peak is also present in **[Pt(II)(DABA)Cl_2]** complex, suggesting that it originates primarily from the Pt(II) coordination environment. Upon incremental addition of GSH (0–80 μM) in 2% DMSO–PBS buffer solution of 10 μM **[Co(III)–**

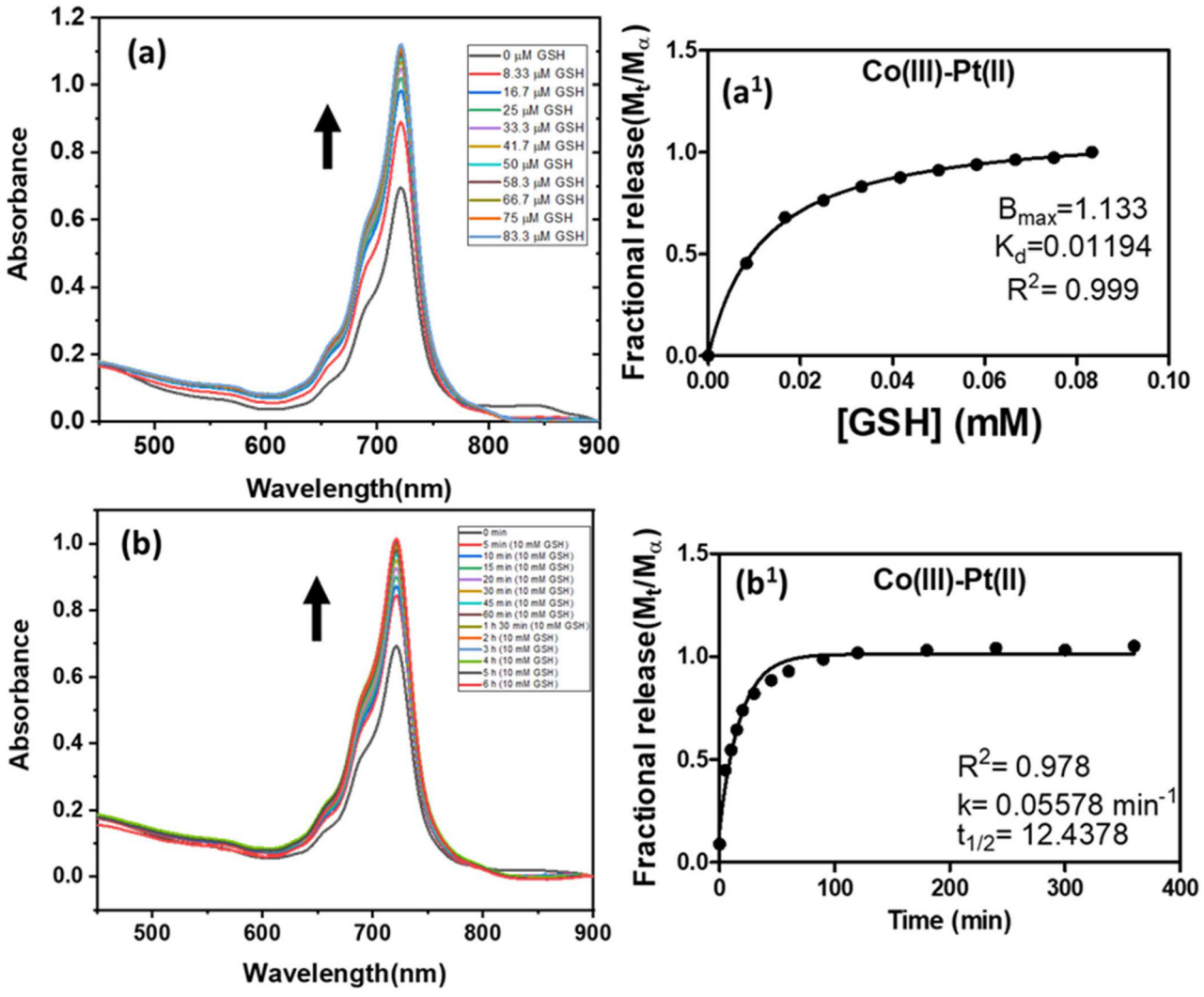

Fig. 1 (a) UV-visible spectroscopic studies of the release of platinum on the addition of increasing amount of GSH (glutathione) in 10 μM of **[Co(III)–Pt(II)]**. The fitting of Fractional release of Pt(II)-complex (M_t/M_α) *vs.* [GSH] using one-site binding model (a^1). (b) UV-visible spectroscopic studies of the release of platinum in the presence of 2.5 μL of 10 mM GSH (glutathione) in 10 μM of **[Co(III)–Pt(II)]** for 6 h. The fitting of Fractional release of Pt(II)-complex (M_t/M_α) *vs.* time (min) using one-site binding model (b^1).

Pt(II)] at pH 5.5, a progressive increase in absorbance intensity at around 710 nm was observed, accompanied by subtle shifts in the spectral profile. The increase in absorbance can be interpreted as an indirect consequence of Co(III) reduction by GSH, which triggers the release of the Pt(II) center, thereby increasing the availability of the Pt(II) complex. The dose-dependent nature of this process was confirmed by plotting fractional release of Pt(II) against GSH concentration, which yielded a saturable one-site binding curve,[55] yielding a B_{max} (maximum achievable release of Pt(II)) of 1.10 and an apparent K_d (GSH concentration required for half-maximal release) of 0.011 mM (Fig. 1a[1]). This suggests a saturable release process governed by a single reduction step. The choice of a one-site binding model is rationalized by the mechanistic pathway of the Co(III) center's reduction by GSH as the critical and saturable step that governs Pt(II) release. Once the coordination site has been reduced and release initiated, additional GSH molecules do not proportionally accelerate the process, resulting in a plateau of the release curve. The dose-dependent saturation profile further confirms that Pt(II) liberation is directly coupled to the redox activity of GSH, a feature of relevance in tumor microenvironments where GSH is typically elevated (1–10 mM).

To further confirm the mechanism of GSH-induced activation and to distinguish between Co(III)-centered reduction and Pt(II)-centered substitution processes, independent UV-Vis titration studies were carried out on **[Co(III)L^1(phen-NH_2)]** and **[Pt(II)(DABA)Cl_2]** in the presence of increasing equivalents of GSH (Fig. S27 and S28). Upon addition of GSH at **[Co(III)L^1(phen-NH_2)]**, a gradual increase in absorbance near 265 nm was observed which is attributed to ligand-centered π–π* transition of phenanthroline, suggesting partial ligand dissociation. Simultaneously, a decrease in intensity in the LMCT region (350–400 nm) is also observed indicating weaking of Co(III) charged transfer transition. This indicates possible reduction of Co(III) to Co(II), accompanied by partial dissociation of the phenanthroline ligand. In contrast, the **[Pt(II)(DABA)Cl_2]** complex exhibited a distinct decrease in the strong absorption band centered around 710 nm upon addition of GSH. This behaviour reflects weakening of the Pt–N chromophore as GSH coordinates to Pt(II) through its thiol group, partially displacing or disrupting the nitrogen-donor environment.[55c] Similar spectral behaviour has been reported for thiol-mediated ligand substitution in Pt(II) complexes, where GSH replaces the chloride ligands to form Pt–S(GSH) adducts.[55c]

Notably, we observed that the **[Co(III)–Pt(II)]** complex shows a different trend, that is an increase in the absorbance of 710 nm band upon GSH addition. The possible explanation of this behaviour is that GSH may first reduce the Co(III) to Co(II), promoting the release of Pt(II) fragment into solution. If such a release occurs, the Pt moiety would no longer be constrained by the cobalt coordination sphere, which may account for the enhancement of absorbance of the 710 nm band. At longer time points, the attenuation of this band could reflect a slower secondary process, such as gradual Pt-thiolate substitution. These results support the notion that GSH reduction of the Co(III) center facilitates ligand release, which may play a key role in the subsequent activation and potential platinum release process in the heterobimetallic Co(III)/Pt(II) complex.

Furthermore, kinetics studies performed using 10 mM GSH in **[Co(III)–Pt(II)]** complex revealed a time-dependent increase in absorbance, which a one-phase exponential association model best described (Fig. 1b[1]).[56] The analysis yielded a rate constant (k) of 0.0558 min^{-1}. The gradual rise in absorbance followed by a plateau demonstrates that the release process is not instantaneous, but proceeds through a controlled first-order kinetic mechanism. This behaviour reflects the reduction-driven activation of the Co(III) centre as the rate-limiting step for Pt(II) liberation. To validate the redox transformation, a cyclic voltammetry (CV) experiment is conducted with increasing GSH concentration (Fig. 2). With the gradual addition of (25–150 μM) GSH, the cathodic peak current decreases, accompanied by a small positive shift in peak potentials $E_{1/2}$ from −0.601 V to −0.555 V. While the magnitude of the potential shift is small, the decrease in the peak current indicates interaction between GSH and the Co(III) complex. It also suggests that GSH stabilised the reduced Co(II) species, making reduction more thermodynamically favourable.

This behaviour is consistent with partial reduction of Co(III) to Co(II) by GSH and the likelihood of GSH to coordinate through its thiol group with the Pt moiety. Additionally, an increase in oxidation current of the irreversible cyclic voltammetric response during anodic scan could be the result of the oxidation of GSH to GSSG. These combined results underline the potential of **[Co(III)–Pt(II)]** to act as a redox-responsive therapeutic platform, selectively activated in the reductive environment of tumor cells.

Reaction of [Co(III)–Pt(II)] with guanosine monophosphate (5′-GMP)

The cytotoxicity of platinum-based compounds is primarily attributed to their ability to bind to DNA, preferentially to the N7 position of guanine among the nucleobases. To investigate these platinum nucleobase interactions, 5′-guanosine monophosphate (5′-GMP) is commonly employed as it effectively mimics the primary DNA binding site while avoiding the complexity of full DNA strands[57] (Fig. 3).

To evaluate the redox-responsive behaviour of **[Co(III)–Pt(II)]** under biomimetic conditions, a one-pot reaction was conducted involving glutathione (GSH) and 5′-GMP. The complex, **[Co(III)–Pt(II)]** (2 mM) was first incubated with 10 mM GSH in 2% DMSO–PBS buffer pH 5.5 for 2 hours to facilitate the reduction of Co(III) centre. Subsequently, 5′-GMP (1 : 1 ratio) was added to the reaction mixture, which was then analysed by mass spectrometry (ESI-MS).[57f] The Q-TOF ESI-MS spectrum exhibits a peak at m/z 612.1514, for the ammonium adduct $[M + NH_4]^+$ of the Pt(II)-ligand fragment $[Pt(II)(C_{19}H_{15}N_5O)Cl_2]$[57g] (Fig. S20 and S32). Additionally, a peak at m/z 351.1207 corresponding to $[Co(II)L^1(H_2O)_2]$ was observed (Fig. S26), consistent with the formation of a reduced cobalt(II) aqua species after

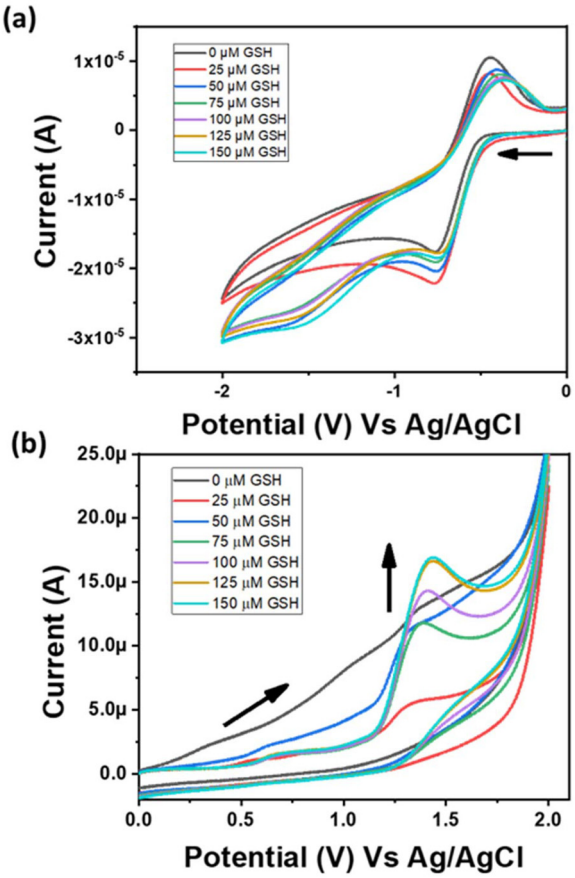

Fig. 2 (a) Cathodic scan in the cyclic voltammogram of **[Co(III)–Pt(II)]** (50 μM) showing the effect of increasing concentration of GSH [25–150 μM] on **[Co(III)–Pt(II)]** in DMF using glassy carbon electrode as working electrode, Ag/AgCl electrode as reference electrode and Pt electrode as counter electrode and TBAP (0.1 M) as supporting electrolyte, at scan rate 50 mV s^{-1}. (b) Anodic scan in the cyclic voltammogram of **[Co(III)–Pt(II)]** showing the effect of increasing concentration of GSH on **[Co(III)–Pt(II)]** in DMF using glassy carbon electrode as working electrode, Ag/AgCl electrode as reference electrode and Pt electrode as counter electrode and TBAP (0.1 M) as supporting electrolyte, at scan rate 50 mV s^{-1}. Increase in oxidation current of the irreversible cyclic voltammetric response during anodic scan could be the result of the oxidation of GSH-assisted *in situ* generated Co(II).

the redox-triggered Pt(II) release. These observation confirms that GSH effectively promotes the reduction of the Co(III) centre, triggering the release of the Pt(II) moiety.

Following reduction and dissociation, the liberated Pt(II)-ligand fragment readily reacts with excess GSH, as evident by a peak at *m*/*z* 845.1719 $[M - Cl]^+$, assigned to a Pt(II)-GSH complex $[Pt(II)(C_{19}H_{15}N_5O)(GSH)Cl]$ (Fig. S21) in which GSH coordinates through its thiol group, displacing a chloride ligand. This demonstrates the reactivity of the Pt(II) complex towards sulfur-containing biomolecules.

A distinct peak at *m*/*z* 906.4011 $[M - OH]^+$ is also observed, which is attributed to a Pt(II)-GMP adduct $[Pt(II)(C_{19}H_{15}N_5O)(GMP)Cl]$ (Fig. S22), indicating successful coordination of GMP to the platinum centre, most likely *via* the N7 position of guanine. Interestingly, a peak at *m*/*z* 280.3149 $[M - PO_4H_2]^{4+}$, M = [Co(III)–Pt(II)Cl(GMP)] (Fig. S23) was also observed, suggesting that the intact complex can associate with GMP even before reduction. However, such binding is limited in extent and likely reflects partial or non-productive association as the Pt(II) coordination environment remains sterically constrained and aquation is suppressed in the substitution-inert Co(III) state. Following GSH-mediated Co(III) to Co(II) reduction, the Pt(II) unit is free, leading to much stronger and more stable Pt-GMP adducts, as evident by the abundant *m*/*z* 906.4 peak. Thus, while pre-reduction interactions are possible, bioreduction significantly enhances the rate and stability of Pt(II) biotransformation, converting weak pre-association into productive DNA-mimic binding.[37b,57]

While previous studies have described glutathione (GSH) as an inactivating agent for platinum-based drugs, due to the formation of strong Pt–S bonds that block Pt–DNA interactions, our results indicate a different role for GSH in this system. Here, GSH functions as a redox activator rather than a detoxifying agent. The thiol-mediated reduction of Co(III) to Co(II) facilitates the release of Pt(II) fragment. Once liberated, the Pt(II) species is able to bind to 5′-GMP, as confirmed by mass spectrometry. Notably, while transient Pt-GSH adducts (*m*/*z* 845.1719) were also detected, such interactions have been reported to be dynamic, and the Pt-GSH conjugates can undergo ligand exchange with competing nucleophiles such as 5′-GMP and exist in equilibria that permit partial regeneration of reactive Pt(II) species under physiological chloride and redox conditions. This shows that several chemical processes in the cell work together to control the behaviour of Pt(II) complex.[57h] Thus, GSH functions simultaneously as an activator of Co(III) reduction and a transient regulator of Pt(II) availability, ultimately enabling the Pt(II) moiety to retain its DNA-binding capacity under reductive tumor conditions.[57]

Cellular uptake study

To investigate the intracellular accumulation of the synthesized **[Co(III)–Pt(II)]** complex in A549 cell lines, time-dependent uptake studies were performed using Inductively Coupled Plasma Mass Spectrometry (ICP-MS). Quantification of platinum (^{195}Pt) and cobalt (^{59}Co) after the treatment of **[Co(III)–Pt(II)]** (10 μM) in A549 cells is done for 0, 3, 6, 12, and 24 hours (Fig. 4 and Table 1). The content of the metal was normalised to a standard cell count 1×10^6 cells per sample, and values were expressed in ng per 10^6 cells. The results showed a biphasic accumulation profile for both metal centres, indicating a time-dependent uptake of both Pt and Co, suggesting a progressive internalisation of the complex. Platinum levels initially increased from 940.8 ng per 10^6 cells at 3 hours to a peak of 1462 ng per 10^6 cells at 12 hours, indicating significant intracellular accumulation. However, at 24 hours, the uptake decreases to 1088 ng per 10^6 cells. Cobalt followed a similar trend, rising from 81.6 to 114.8 ng per 10^6 cells before declining to 81.2 ng per 10^6 cells.

Although both metals displayed comparable time-dependent patterns, the consistently higher intracellular accumu-

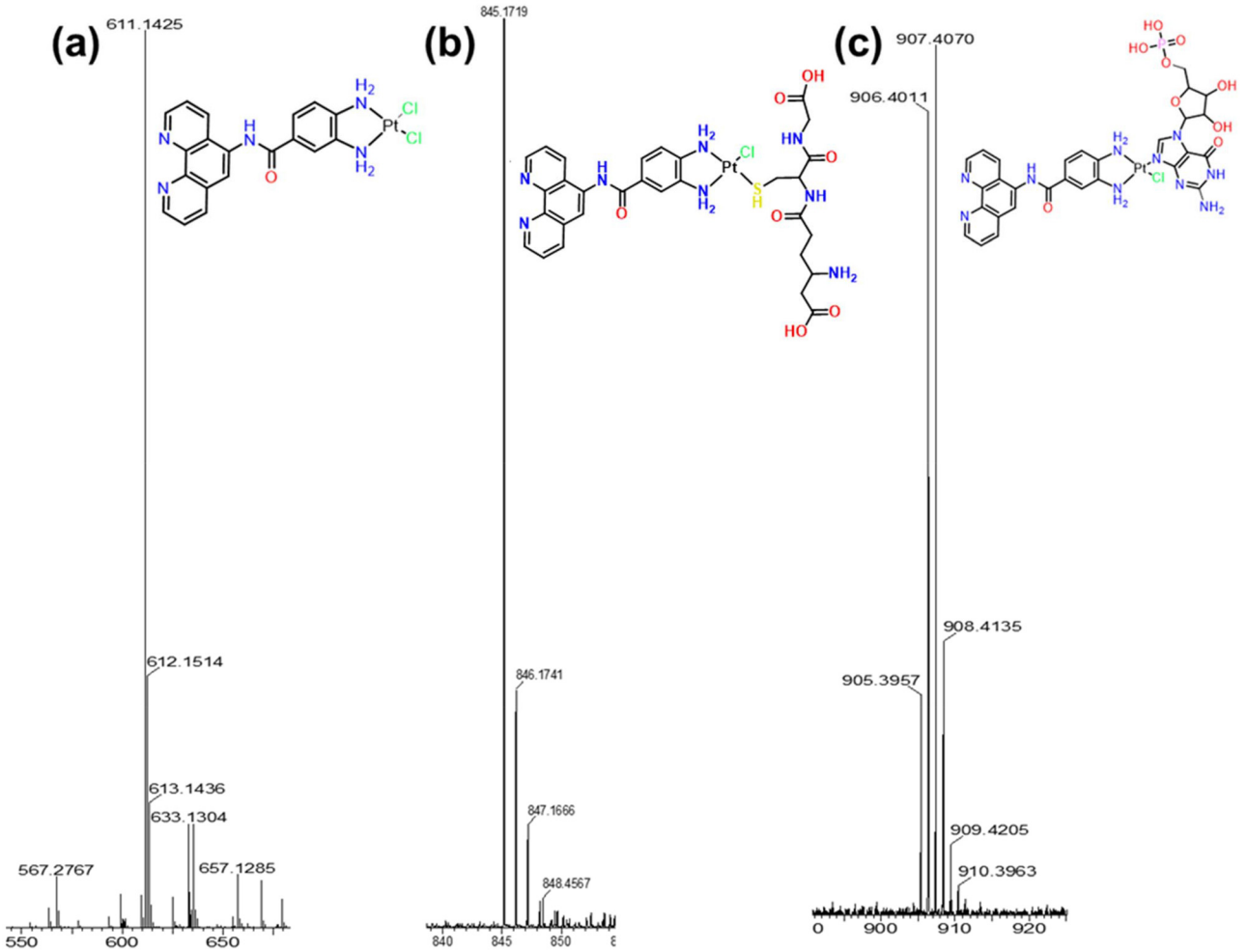

Fig. 3 Q-TOF ESI Mass spectra of the complex, **[Co(III)–Pt(II)]** while incubated with 5′-guanosine monophosphate (5′-GMP) in the presence of 10 mM GSH in CH_3OH recorded using Waters Micromass Q-Tof Micro spectro-photometer. (a) *m/z* 612.1514 corresponds to the $[M + NH_4]^+$ ion of the Pt(II) fragment, where M = $[Pt(II)(C_{19}H_{15}N_5O)Cl_2]$, and *m/z* 611.1425 corresponds to the isotopic pattern of the $[M + NH_4]^+$ ion. (b) *m/z* 845.1719 $[M - Cl]^+$, is assigned to a Pt(II)-GSH complex $[Pt(II)(C_{19}H_{15}N_5O)(GSH)Cl]$, and (c) *m/z* 906.4011 $[M - OH]^+$ is attributed to a Pt(II)–GMP adduct $[Pt(II)(C_{19}H_{15}N_5O)(GMP)Cl]$ after reduction of Co(III) to Co(II).

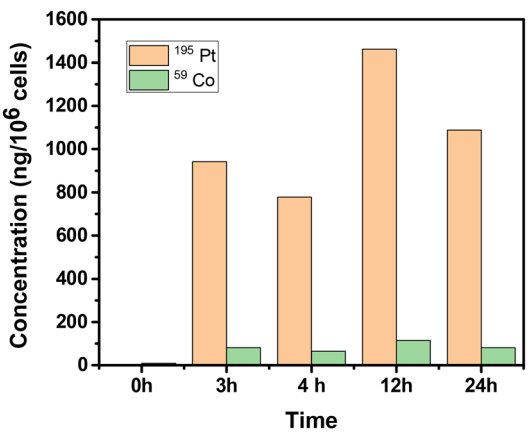

Fig. 4 Bar diagram showing the quantification of intracellular ^{159}Pt and ^{59}Co by the ICPMS method after the complex, **[Co(III)–Pt(II)]** was uptake in A549 cells. Data are expressed as nanograms of Pt and Co per 10^6 cells.

Table 1 Cellular uptake the complex, **[Co(III)–Pt(II)]** in A549 cells probed by inductively coupled plasma mass spectrometry (ICP-MS)

Time (h)	^{195}Pt (ng per 10^6 cells)	^{59}Co (ng per 10^6 cells)
0	0.40 ± 0.03	8.00 ± 0.9
3	940.8 ± 0.02	81.6 ± 0.3
6	778.4 ± 0.1	64.4 ± 0.01
12	1462.0 ± 2.2	114.8 ± 0.03
24	1088.0 ± 1.1	81.2 ± 0.2

lation of Pt levels likely reflects the differences in their intracellular fates. Pt is known to form irreversible covalent binding with nucleophilic biomolecules such as DNA and proteins, leading to enhanced retention. At the same time, Co(III) can undergo redox activation to Co(II), which is more labile and may undergo ligand exchange, followed by possible efflux, reducing its net accumulation. This overall biphasic pattern is consistent with previous observations for platinum-based com-

plexes and likely reflects a dynamic balance between cellular uptake and clearance mechanisms.

During the early time points, the bimetallic **[Co(III)–Pt(II)]** may be internalized through passive diffusion, active transport, or endocytic pathways, leading to progressive accumulation within intracellular compartments. Similar uptake kinetics have been reported for cisplatin and other platinum compounds, which accumulate rapidly inside cancer cells due to their physicochemical properties and high affinity for nucleophilic sites. Following peak accumulation, the subsequent decline may result from a combination of active efflux, metabolic transformation, and cellular adaptive responses. For instance, ATP-binding cassette (ABC) transporters such as MRP2 and ATP7B mediate platinum species' active efflux, contributing to drug clearance and resistance.[58] The observed peak accumulation at 12 hours suggests that this time point may correspond to the window of maximal pharmacological activity, highlighting its potential relevance for dosing strategies. Furthermore, the strong correlation between Pt and Co uptake suggests the complex is internalised as a structurally intact species, without significant dissociation in the extracellular environment. Maintaining this structural integrity during cellular uptake ensures that the redox-controlled delivery mechanism is preserved, enabling selective activation of cytotoxic platinum species within the reductive environment of cancer cells.

Cell viability assay

The cell viability assay of all three complexes was evaluated using the MTT assay across different cell lines, including A549 (human alveolar basal epithelial cells), MDA-MB-231 (human breast adenocarcinoma), MCF-7 (human breast cancer), HT-29 (human colon adenocarcinoma), and HaCaT (human immortalized keratinocytes). A549 cells were also assessed under hypoxic conditions to mimic the tumour microenvironment.

Cells were seeded at a density of 6000–8000 cells per well in 96-well plates, with a total volume was 100 μL per well. Treatments were administered at varying concentrations over 24, 48, and 72 hours, and each condition was performed in triplicate in the A549 cell line. IC_{50} values were calculated by non-linear regression analysis using GraphPad Prism software, based on %cell viability *vs.* log[concentration] plot (Fig. 5, Fig. S24, Fig. S25 and Table 2).

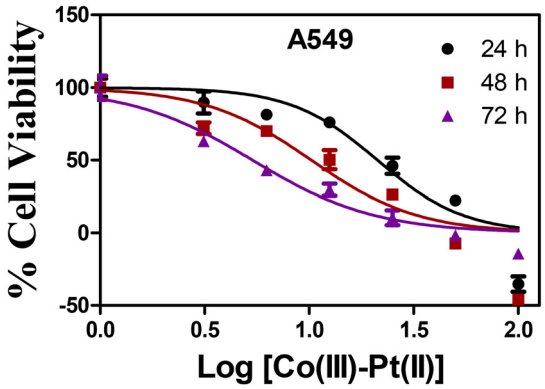

Fig. 5 Plot of cell viability *vs.* [Co(III)–Pt(II)] and non-linear regression fitting of cellular viability data in A549 cell lines. Viability decreases as the log concentration of the complexes increases, indicating their dose-dependent activity. Data are presented as mean ± standard deviation.

Among the tested compounds, the **[Co(III)–Pt(II)]** complex exhibited the most potent cytotoxic activity across all cell lines. In A549 cells, the IC_{50} values progressively decreased from 21.21 μM at 24 h to 5.364 μM at 72 h, indicating a time-dependent enhancement in cytotoxic effect. Notably, this complex also demonstrates high potency against MDA-MB-231 cell lines (IC_{50} = 9.508 μM) and maintains efficacy under hypoxic conditions, suggesting that the compound retains activity even in tumour-mimicking microenvironments. Moreover, the **[Co(III)–Pt(II)]** exhibited moderate toxicity in non-cancerous HaCaT cells and HT-29, indicating a degree of cancer cell selectivity. In contrast, **[Pt(II)(DABA)Cl_2]** complex showed significantly reduced cytotoxicity, potentially due to limited cellular uptake and insufficient DNA interaction. Notably, while **[Pt(II)(DABA)Cl_2]** has been previously reported to exhibit an IC_{50} of 89 μM in K562 leukemic cells at 24 h, our study demonstrates significant improvement in cytotoxicity in A549 cells at 72 h (IC_{50} = 13.41 μM). On the other hand, the **[Co(III)(L^1)(phen-NH_2)](acac)$_3$** complex remained minimally toxic across

Table 2 IC_{50} values determined by non-regression analysis of %cell viability *vs.* log[concentration] plot in different cancer cell lines treated with different concentrations of the complexes

Complexes	A549 (μM)			MDA-MB-231[a] (μM)	HaCaT[a] (μM)	HT-29[a] (μM)	A549[a] (hypoxia) (μM)	MCF-7[a] (μM)
	24 h	48 h	72 h					
[Co(III)–Pt(II)]	21.21 ± 0.1	10.25 ± 0.5	5.364 ± 0.1	9.51 ± 0.4	35.15 ± 0.2	25.02 ± 0.7	14.09 ± 0.4	17.53 ± 0.1
[Pt(II)(DABA)Cl_2]	>70	>50	13.41 ± 0.1	>50	>50	>50	>100	>50
[Co(III)(L^1)(phen-NH_2)](acac)$_3$	>200	>100	40.72 ± 0.2	>100	>100	>100	>60	>70
L^1	>200							
L^2	>100							
***cis*-Platin**	21.29							

[a] Cells were treated with the compounds for 24 h.

all tested conditions. Overall, these findings demonstrate that **[Co(III)–Pt(II)]** is a potent redox-responsive anticancer agent with selective cytotoxicity across multiple cancer cell lines, including hypoxia.

Real-time reverse transcription-polymerase chain reaction (RT-PCR)

Quantitative real time RT-PCR was employed to assess the transcriptional levels of hypoxia-inducible factor 1-alpha (HIF-1α) and its downstream targets, vascular endothelial growth factor (VEGF) and glucose transporter 1 (GLUT-1) in MDA-MB-231 breast cancer cells treated with **[Co(III)–Pt(II)]** complex (7.3 μM). The fold change data revealed a significant downregulation of all three target genes, indicating that the complex effectively disrupts hypoxia-mediated signalling pathways associated with tumor progression (Fig. 6).

HIF-1α functions as a central transcriptional regulator under hypoxic conditions. It binds to hypoxia response elements (HREs) in the promoter regions of target genes and drives the expression of factors responsible for oxygen homeostasis, metabolic adaptation, and cell survival to hypoxic stress. The downstream target genes VEGF plays an important role in promoting angiogenesis by stimulating new blood vessel formation, ensuring an adequate oxygen and nutrient supply to growing tumors. GLUT-1 also facilitates the uptake of glucose to increase anaerobic glycolysis, a major source of ATP under hypoxic stress.[59] Downregulation of HIF-1α disrupts the hypoxia-inducible signal, impairing the transcription of VEGF and GLUT-1. As a result, the suppression of VEGF expression limits the formation of new blood vessels, making the cell more oxygen-deprived, while decreased GLUT-1 expression limits glucose uptake and energy production, reducing the tumor's metabolic resilience. The **[Co(III)–Pt(II)]** may mediate these effects by altering intracellular redox balance, promoting HIF-1α degradation, or hindering the interaction between HIF-1α and its co-activators. This coordinated downregulation of gene impairs the tumor's ability to adapt to hypoxic stress, highlighting the potential of the **[Co(III)–Pt(II)]** as a promising therapeutic agent that targets the hypoxia-driven pathways in cancer.

Annexin V/PI assay

Apoptosis, or programmed cell death, is crucial for maintaining tissue homeostasis and represents a key target for anticancer therapies. A characteristic feature of apoptosis is the externalization of phosphatidylserine from the inner to the outer leaflet of the plasma membrane. Concurrently, loss of membrane integrity at later stages allows uptake of DNA-binding dyes such as propidium iodide (PI).

To determine whether the observed cytotoxic effect of the **[Co(III)–Pt(II)]** results from apoptosis, a dual-staining Annexin V-FITC/PI assay was conducted and analysed *via* flow cytometry. In the untreated control cells, viability remains high, whereas the treatment of **[Co(III)–Pt(II)]** induced a marked decrease in viable cells. The increase in Annexin V^+/PI^- population indicates early apoptotic events marked by phosphatidylserine externalization, while the rise in Annexin V^+/PI^+ cells signify progression to late-stage apoptosis or secondary necrosis. The negligible necrotic fraction (0.28%) further supports the specificity of the apoptotic pathway activation rather than non-specific membrane disruption (Fig. 7). Overall, these findings demonstrate that the treatment effectively induces apoptotic cell death and confirm the pro-apoptotic potential of the compound and provide preliminary mechanistic insights into its cytotoxic mode of action.

Scratch wound healing assay

The scratch wound healing assay was conducted to assess the anti-migratory effect of **[Co(III)–Pt(II)]** in MDA-MB-231 breast cancer cells. This assay provides a method to evaluate cell migration, a key process involved in wound healing, tissue regeneration, and cancer metastasis.[60] A uniform linear scratch in a confluent monolayer of cells was created and treated with **[Co(III)–Pt(II)]** (7.2 μM) to monitor how effectively cells moved to close the wound area (Fig. 8). Quantitative analysis was performed using ImageJ software, and the percentage of wound closure was calculated by comparing the wound area at 24 hours to the initial area at 0 hours. The untreated control group exhibited a wound closure percentage of 45.64%, indicating active cell migration. In contrast, cells treated with **[Co(III)–Pt(II)]** showed a significantly lower wound healing percen-

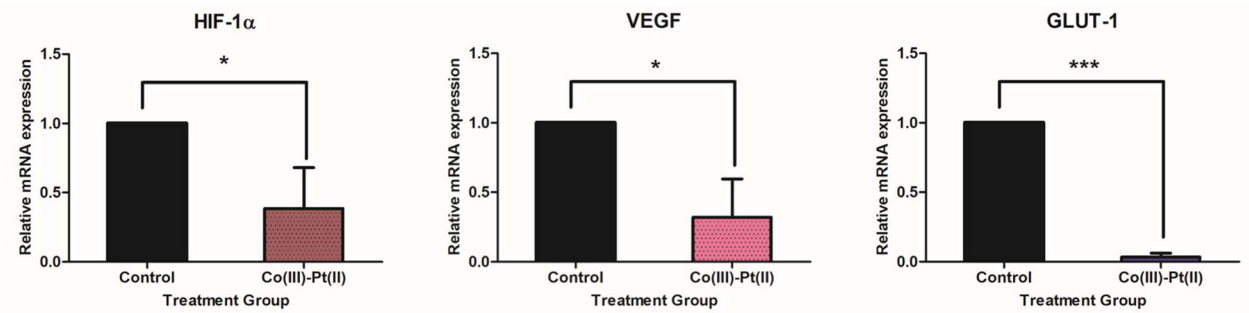

Fig. 6 q-RT-PCR analysis of (A) HIF-1α, (B) VEGF, and (C) GLUT-1 mRNA expression levels in tumour samples in **[Co(III)–Pt(II)]** treated cells with internal control β-actin. Expression levels were normalized to control. Data are presented as mean ± SD. *$P < 0.05$, ***$p < 0.001$.

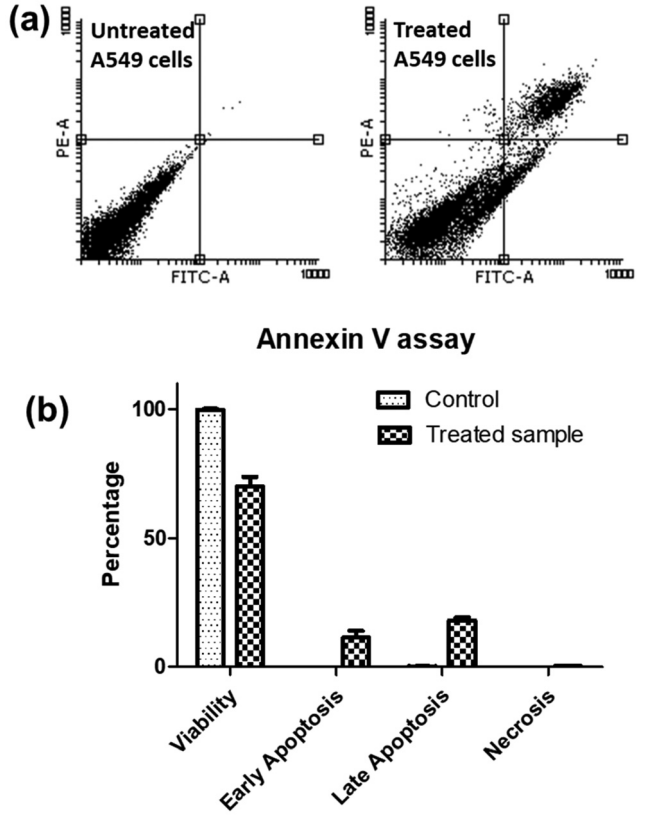

Fig. 7 (a) Annexin-V-FITC/PI assay of A549 cells incubated with **[Co(III)–Pt(II)]** for 24 h. Flow cytometry analysis was performed to distinguish between viable cells (Annexin V^-/PI^-), early apoptotic cells (Annexin V^+/PI^-), late apoptotic (Annexin V^+/PI^+), and necrotic cells (Annexin V^-/PI^+). Representative dot plots are shown for each treatment group. (b) Bar diagram representing the quantitative population of the nature of A549 cells.

tage of 9.02%, suggesting a strong inhibitory effect on cell migration. This reduction in the migratory activity implies that the complex may interfere with the cellular mechanism regulating migration. Statistical analysis using one-way ANOVA confirmed that the difference in wound healing between the treated and control groups was statistically significant ($p < 0.05$). These finding supports the potential of **[Co(III)–Pt(II)]** complex as a migratory-inhibiting agent with possible applications in suppressing cancer cell metastasis.

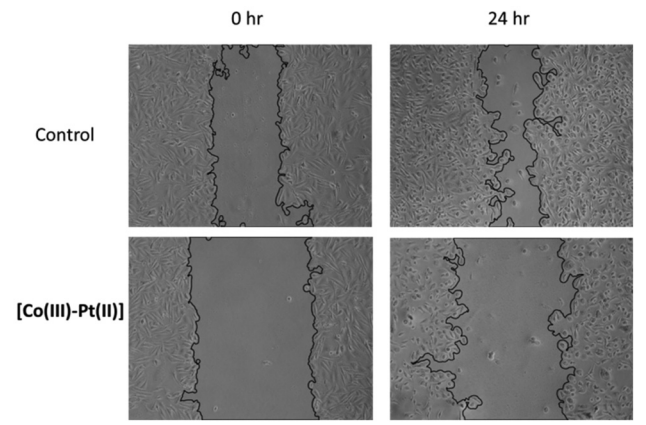

Fig. 8 Scratch wound healing assay showing inhibition of cell migration in MDA-MB-231 cells upon treatment with **[Co(III)–Pt(II)]** complex for 24 hours. Compared to the control group, treated cells exhibited reduced wound closure. Images were captured at 0 and 24 hours.

Experimental

Materials and methods

All reagents and solvents employed for the synthesis were acquired from reputable commercial suppliers. Tris(acetylacetonato)cobalt(III), 5-amino-1,10-phenanthroline, potassium tetrachloroplatinate(II), 3,4-diaminobenzoic acid, pyridine-2-carboxaldehyde, ethylenediamine, cobalt chloride 1-ethyl-3-(3-dimethylaminopropyl)carbodiimide (EDC·HCl), 1-hydroxybenzotriazole (HOBt), glutathione (GSH), 5′-GMP and MTT were purchased from Sigma-Aldrich, DMEM media (MP Biomedicals), Penicillin (Gibco), Streptomycin (Gibco), Fetal Bovine Serum (Gibco), Trypsin EDTA (Sigma-Aldrich), 6 well plates (Tarsons), MTT [3-(4,5-dimethylthiazol-2-yl)-2,5-diphenyltetrazolium bromide] Reagent (Invitrogen), Cell culture grade DMSO (MP Biomedicals), Trizol (Thermo Fisher Cat. no: 15596026), cDNA synthesis kit (Thermo Scientific Cat no. K1622), SYBR green (Invitrogen-ABI Cat no. A25742). Other chemicals and solvents were obtained from SRL, HI-MEDIA, and TCI chemicals and used without purification. All cell lines were from ATCC and the National repository (National Centre for Cell Science, Pune, India).

UV-visible spectra were recorded using PerkinElmer UV-vis, Fourier transform infrared (FT-IR) spectra were recorded using PerkinElmer UATR two FT-IR, and photoluminescence spectra were recorded using a Hitachi F-7000 fluorescence spectrophotometer. The ^{1}H NMR spectra were recorded on a Bruker Avance 400 (400 MHz) NMR spectrometer using DMSO-d_6 as solvent and internal standard as tetramethylsilane (TMS). The Q-TOF-ESI mass spectra were recorded in Bruker Esquire 3000 Plus spectrometer. Elemental analysis was performed in A PerkinElmer 2400 series II elemental analyzer. The absorbance readings in MTT assays were performed using Cytation 5, BioTek microplate reader. The cellular uptake of compounds was studied by using Agilent 7850 Inductively Coupled Plasma Mass Spectrometry (ICPMS) instrument. For RT-PCR analysis, RNA concentration and purity were measured using a NanoDrop Spectrophotometer.

Synthesis

Synthesis of L^1 [*N*,*N*-(ethane-1,2-diyl)bis(1-(pyridine-2-yl)methanimine)]. Ligand L^1 was synthesized using pyridine-2-carboxaldehyde and ethylenediamine with minor modification as per the protocol reported previously.[46] The reaction mixture was kept for 6 h in reflux and cooled at room temperature. The yellow colour crystal was washed with hexane. The characteristics data of the compound were matched with the reported values.

Synthesis of [Co(III)(L^1)(phen-NH_2)][acac]$_3$. Methanolic solution of ligand L^1 (0.287 mmol, 68.39 mg) was added to a methanolic solution (5 mL) of Tris(acetylacetonato)cobalt(III) [$Co(C_5H_7O_2)_3$] (0.287 mmol, 102.24 mg), followed by addition of L^2 (5-amino-1,10-phenanthroline) (0.287 mmol, 56.32 mg). The reaction mixture was refluxed for 6 h with constant stirring. The resulting solution was kept for slow evaporation at room temperature to obtain a brownish precipitate. The product was filtered and washed with hexane and diethyl ether. The product was characterized by UV-visible, FT-IR, ^{1}H NMR and mass spectrometry.

$C_{26}H_{23}CoN_7$: colour: reddish brown; elemental analysis (%) calculated C, 63.41; H, 4.71; N, 19.91; found C, 63.37; H, 4.80; N, 19.57; UV-visible spectra in 2% DMSO/H_2O [λ_{max}, nm]: 264 (π–π^*), 300 (LMCT), 444 (d–d transition); FT-IR spectra, solid phase: ν (cm^{-1}): (C═N_{str}, N–H_{str}) 1650, 3130; ^{1}H NMR (400 MHz, DMSO-d_6) δ 9.42–9.04 (m, 1H), 8.67–8.28 (m, 4H), 8.15 (q, 1H), 7.94 (s, 2H), 7.85–7.53 (m, 4H), 7.48–7.37 (m, 1H), 7.32–7.11 (m, 4H), 7.04 (s, 1H), 6.62 (s, 1H), 2.96–2.67 (m, 4H); Q-TOF ESI mass analysis in CH_3OH: m/z 164.0366 corresponds to the species $[M]^{3+}$ of **[Co(III)(L^1)(phen-NH_2)]**. The isolated product was obtained in 90.7 mg (64.2% yield).

Synthesis of [Pt(II)(DABA)Cl_2]. **[Pt(II)(DABA)Cl_2]** was synthesized as per the protocol reported previously. A dimethylformamide solution of 3,4-diaminobenzoic acid (0.287 mmol, 43.7 mg) was added to an aqueous solution (5 mL) of potassium tetrachloroplatinate(II) [K_2PtCl_4] (0.287 mmol, 119.1 mg) and stirred at room temperature for 8 hours. A dark, bluish-green solution was obtained. The solution was filtered and then rotary-evaporated to obtain the final product. The product was washed with diethyl ether and characterized by UV-visible spectroscopy, FT-IR, ^{1}H NMR and mass spectrometry. $C_7H_8Cl_2N_2O_2Pt$: colour: royal blue; elemental analysis (%) calculated C, 20.11; H, 1.93; N, 6.70; found C, 20.04; H, 2; N, 6.74; UV-visible spectra in 2% DMSO/H_2O [λ_{max}, nm]: 314, 278 (π–π^*), 712 (MLCT); FT-IR spectra, solid phase: ν (cm^{-1}): (O–H_{str}, N–H_{str}, C–N_{str}, C═O_{str}) 1710–1720; ^{1}H NMR (400 MHz, DMSO-d_6) δ 12.00 (s, 1H), 7.23 (d, 1H), 7.17 (dd, 1H), 6.55 (d, 1H), 5.46 (s, 4H); Q-TOF ESI mass analysis in CH_3OH: m/z 380.9736 corresponds to the species [M − Cl − H]$^+$ of **[Pt(II)(DABA)Cl_2]**. The isolated product was obtained in 54.7 mg (45.6% yield).

Synthesis of [Co(III)–Pt(II)][acac]$_3$ ([Co(III)–Pt(II)]). **[Pt(II)(DABA)Cl_2]** complex is dissolved in DMF and kept in an ice bath. HOBt (1.1 eq.) and EDC.HCl (1.2 eq.) is added to the solution and is kept for 30 minutes. After that, **[Co(III)(L^1)(phen-NH_2)][acac]$_3$** solution in DMF is added and continues stirring at room temperature for 12 hours. The resulting solution is rotary evaporated and processed with dichloromethane (DCM) and water to ensure complete reaction and purification. The product was characterized by UV-Vis spectroscopy, FT-IR, ^{1}H NMR, and Mass. $C_{33}H_{29}Cl_2CoN_9OPt$: colour: reddish brown; elemental analysis (%) calculated C, 44.41; H, 3.28; N, 14.12; found C, 44.24; H, 3.31; N, 14.08; UV-visible spectra in 2% DMSO/H_2O [λ_{max}, nm]: 278 (π–π^*), 307 (LMCT), 445 (d–d transition), 723 (MLCT); FT-IR spectra, solid phase: ν (cm^{-1}): (C═N_{str}, C═O_{str}, N–H_{str}) 1656, 1669, 3130; ^{1}H NMR (400 MHz, DMSO-d_6) δ 10.26 (s, 1H), 9.40–8.91 (m, 2H), 8.81–8.44 (m, 4H), 8.27–8.08 (m, 2H), 8.01–7.86 (m, 2H), 7.74 (s, 2H), 7.58 (s, 1H), 7.34 (dd, 4H), 7.11 (dd, 2H), 6.82 (d, 1H), 5.63 (s, 4H), 2.98–2.65 (m, 4H); Q-TOF ESI mass analysis in CH_3OH: m/z 297.1471 corresponds to the species $[M]^{3+}$ of **[Co(III)–Pt(II)]**. The isolated product was obtained in 0.506 g (56.7% yield).

Conclusions

In summary, we have successfully designed and synthesized a redox-responsive heterobimetallic complex, **[Co(III)–Pt(II)]** complex that exploits the tumor-associated reductive microenvironment for selective activation of Co(III) and release of Pt(II). Comprehensive spectroscopic and electrochemical analyses revealed a quasi-reversible one-electron reduction of the Co(III) center under biologically relevant conditions, enabling the reductive release of the Pt(II) fragment. Binding studies with 5′-GMP confirmed the liberated Pt(II) species engages in cross-linking to DNA, thereby providing a mechanistic basis for its cytotoxic activity. Cellular uptake experiments demonstrated efficient internalization, while Annexin-V assays verified apoptosis induction. Importantly, the complex exhibited potent cytotoxicity across wide range of cancer cell lines, including drug-resistant phenotypes, under both normoxic and hypoxic conditions. These findings highlight the potential of redox-activated bimetallic architectures as next-generation metalloprodrugs, capable of enhancing tumor selectivity, overcoming platinum resistance, and reducing systemic toxicity relative to conventional platinum chemotherapeutics.

Author contributions

Sharmila Wahengbam: synthesis and characterization, physico-chemical assays, kinetics study, writing original draft; Neha Masarkar: MTT assay in MDA-MB-231, RT-PCR, wound healing assay; Himanshi Sharma: MTT assays in A549, hypoxic A549, HT-29, HaCaT; Sukhes Mukherjee: supervision; Chandi Charan Malakar: supervision; Mithun Roy: conceptualization, fund accumulation, supervision of the work, writing original draft, and editing.

Conflicts of interest

There are no conflicts to declare.

Data availability

The data supporting this article have been included as part of the supplementary information (SI). Supplementary information is available. See DOI: https://doi.org/10.1039/d5dt02296g.

Acknowledgements

Indian Council of Medical Research (ICMR) (R.11.13/42/2021 GIA/HR ICMR) and Innovation in Science Pursuit for Inspired Research (INSPIRE) Fellowship program (DST-INSPIRE FELLOWSHIP/2019/IF190850) for financial support and NIT Manipur for providing infrastructure. We also thank Punjab University and the University of Delhi for their assistance with characterisation. We sincerely thank Dr Manoj B. Menon of the Kusuma School of Biological Sciences, IIT Delhi, for providing the facility for performing MTT. We also thank Krushnapriya Samantara for helping in this study.

References

1 Y. Guo, F. Gao, A. Ahmed, M. Rafiq, B. Yu, H. Cong and Y. Shen, *J. Mater. Chem. B*, 2023, **11**, 8586–8604.
2 G. Jiang, Z. Xiang and Q. Fang, *Nanoscale Horiz.*, 2023, **8**, 1062–1072.
3 H.-Y. Min and H.-Y. Lee, *Exp. Mol. Med.*, 2022, **54**, 1670–1694.
4 L. Galluzzi, M. J. Aryankalayil, C. N. Coleman and S. C. Formenti, *Nat. Rev. Clin. Oncol.*, 2023, **20**, 543–557.
5 A. Zafar, M. J. Khan, J. Abu and A. Naeem, *Mol. Biol. Rep.*, 2024, **51**, 219.
6 S. Sharma, C. Kumar, H. Kushwaha, S. K. Jha, S. Chawla, A. Sharma, T. Midha and V. Huddar, *Ayush J. Integr. Oncol.*, 2025, **2**, 8–27.
7 Y. Yue, Y. Ren, C. Lu, N. Jiang, S. Wang, J. Fu, M. Kong and G. Zhang, *Discover Oncol.*, 2025, **16**, 1–19.
8 S. Alassadi, M. J. Pisani and N. J. Wheate, *Dalton Trans.*, 2022, **51**, 10835–10846.
9 S. R. E. Mason, M. L. Willson, S. J. Egger, J. Beith, R. F. Dear and A. Goodwin, *Cochrane Database Syst. Rev.*, 2023, **9**, CD013452.
10 C. M. Allen, F. Lopes, R. T. Mitchell and N. Spears, *Mol. Hum. Reprod.*, 2020, **26**, 129–140.
11 T. Makovec, *Radiol. Oncol.*, 2019, **53**, 148.
12 Z. Y. Ma, X. J. Ding, Z. Z. Zhu, Q. Chen, D. B. Wang, X. Qiao and J. Y. Xu, *RSC Med. Chem.*, 2024, **15**, 3239–3247.
13 P. B. Tchounwou, S. Dasari, F. K. Noubissi, P. Ray and S. Kumar, *J. Exp. Pharmacol.*, 2021, **13**, 303–328.
14 C. Zhang, C. Xu, X. Gao and Q. Yao, *Theranostics*, 2022, **12**, 2115–2132.
15 T. W. Hambley, *J. Chem. Soc., Dalton Trans.*, 2001, 2711–2718.
16 Y. Roque-Diaz, M. Sanadar, D. Han, M. Lopez-Mesas, M. Valiente, M. Tolazzi, A. Melchior and D. Veclani, *Processes*, 2021, **9**, 1873.
17 R. Oun, Y. E. Moussa and N. J. Wheate, *Dalton Trans.*, 2018, **47**, 6645–6653.
18 S. Dilruba and G. V. Kalayda, *Cancer Chemother. Pharmacol.*, 2016, **77**, 1103–1124.
19 C. Lin, J. Cui, Z. Peng, K. Qian, R. Wu, Y. Cheng and W. Yin, *Eur. J. Med. Res.*, 2022, **27**, 201.
20 A.-M. Florea and D. Büsselberg, *Cancers*, 2011, **3**, 1351–1371.
21 X. Ling, J. Tu, J. Wang, A. Shajii, N. Kong, C. Feng, Y. Zhang, M. Yu, T. Xie, Z. Bharwani and B. M. Aljaeid, *ACS Nano*, 2019, **13**, 357–370.
22 D. J. Stewart, *Crit. Rev. Oncol. Hematol.*, 2007, **63**, 12–31.
23 B. A. J. Jansen, J. Brouwer and J. Reedijk, *J. Inorg. Biochem.*, 2002, **89**, 197–202.
24 G. E. Valenti, B. Tasso, N. Traverso, C. Domenicotti and B. Marengo, *Redox Exp. Med.*, 2023, **2023**, e220023.
25 M. Abdelsalam, M. Zmyslia, K. Schmidtkunz, A. Vecchio, S. Hilscher, H. S. Ibrahim, M. Schutkowski, M. Jung, C. Jessen-Trefzer and W. Sippl, *Arch. Pharm.*, 2024, **357**, 2300536.
26 C. P. Guise, A. M. Mowday, A. Ashoorzadeh, R. Yuan, W.-H. Lin, D.-H. Wu, J. B. Smaill, A. V. Patterson and K. Ding, *Chin. J. Cancer*, 2014, **33**, 80.
27 C. Tosun, A. L. D. Wallabregue, M. Mallerman, S. E. Phillips, C. M. Edwards, S. J. Conway and E. M. Hammond, *JACS Au*, 2023, **3**, 3237–3246.
28 D.-C. Yang, L.-F. Wen, L. Du, C.-M. Luo, Z.-Y. Lu, J.-Y. Liu and Z. Lin, *ACS Appl. Mater. Interfaces*, 2022, **14**, 40546–40558.
29 S. Wahengbam, H. Sharma, P. R. Chanu, N. Masarkar, S. Mukherjee, M. B. Menon, C. C. Malakar and M. Roy, *RSC Med. Chem.*, 2025, **16**, 5382–5394.
30 L. Larasati, W. W. Lestari and M. Firdaus, *Bull. Chem. Soc. Jpn.*, 2022, **95**, 1561–1577.
31 A. Skoczynska, A. Lewinski, M. Pokora, P. Paneth and E. Budzisz, *Int. J. Mol. Sci.*, 2023, **24**, 9512.
32 J. L. Quiles, C. Sanchez-Gonzalez, L. Vera-Ramirez, F. Giampieri, M. D. Navarro-Hortal, J. Xiao, J. Llopis, M. Battino and A. Varela-López, *Antioxid. Redox Signal.*, 2020, **33**, 860–881.
33 X. Yuan, Z. Xie and T. Zou, *Bioorg. Chem.*, 2024, **144**, 107161.
34 S. Chen, Q. Zhou, K. Ng, Z. Xu, W. Xu and G. Zhu, *Inorg. Chem. Front.*, 2024, **11**, 3085–3118.
35 U. Jungwirth, C. R. Kowol, B. K. Keppler, C. G. Hartinger, W. Berger and P. Heffeter, *Antioxid. Redox Signal.*, 2011, **15**, 1085–1127.
36 X. Zhong, Y. Zhang and J. Wei, *Drug Dev. Ind. Pharm.*, 2025, **51**, 169–179.
37 (*a*) A. Levina, D. C. Crans and P. A. Lay, *Pharmaceutics*, 2022, **14**, 790; (*b*) T. W. Failes and T. W. Hambley, *Dalton Trans.*, 2006, 1895–1901; (*c*) T. W. Failes, C. Cullinane, C. I. Diakos, N. Yamamoto, J. G. Lyons and T. W. Hambley, *Chem. – Eur. J.*, 2007, **13**, 4513–4526.
38 I. C. A. de Souza, S. de Souza Santana, J. G. Gómez, G. P. Guedes, J. Madureira, S. M. de Ornelas Quintal and M. Lanznaster, *Dalton Trans.*, 2020, **49**, 16425–16439.
39 G. Genchi, G. Lauria, A. Catalano, A. Carocci and M. S. Sinicropi, *Biology*, 2023, **12**, 1335.
40 A. Bera, A. Nepalia, A. Upadhyay, D. K. Saini and A. R. Chakravarty, *Inorg. Chem.*, 2024, **63**, 17249–17262.
41 J. Karges, T. Yempala, M. Tharaud, D. Gibson and G. Gasser, *Angew. Chem., Int. Ed.*, 2020, **59**, 7069–7075.
42 S. Scoditti, G. Mazzone, N. Sanna and E. Sicilia, *Inorg. Chem.*, 2022, **61**, 12903–12912.

43 A. Herman, S. D. Shnyder, A. A. Phillips, B. Patel, M. J. Tilby, G. R. Pettit, P. J. Smith, R. J. Knox and J. A. Parkinson, *Inorg. Chem.*, 2008, **47**, 602–611.
44 A. Gupta, A. K. Pandey, T. Mondal, J. Bhattacharya and P. K. Sasmal, *J. Med. Chem.*, 2023, **66**, 8687–8704.
45 T. B. Tran, É. Sipos, A. C. Bényei, S. Nagy, I. Lekli and P. Buglyó, *Molecules*, 2024, **29**, 5967.
46 G. Amenuvor, C. K. Rono, J. Darkwa and B. C. E. Makhubela, *Eur. J. Inorg. Chem.*, 2019, 3942–3953.
47 E. C. Sutton, C. E. McDevitt, J. Y. Prochnau, M. V. Yglesias, A. M. Mroz, M. C. Yang, R. M. Cunningham, C. H. Hendon and V. J. DeRose, *J. Am. Chem. Soc.*, 2019, **141**, 18411–18415.
48 Q.-L. Zhang, J.-G. Liu, H. Chao, G.-Q. Xue and L.-N. Ji, *J. Inorg. Biochem.*, 2001, **83**, 49–55.
49 (*a*) N. Jain and T. S. Srivastava, *Indian J. Chem., Sect. A*, 1992, **31**, 102–105; (*b*) Y. H. Zhao and M. H. Abraham, *J. Org. Chem.*, 2005, **70**, 2633–2640.
50 E. S. Wiedner, J. A. S. Roberts, W. G. Dougherty, W. S. Kassel, D. L. DuBois and R. M. Bullock, *Inorg. Chem.*, 2013, 52, 9975–9988.
51 P. Daubinger, J. Kieninger, T. Unmüssig and G. A. Urban, *Phys. Chem. Chem. Phys.*, 2014, **16**, 8392–8399.
52 O. A. González-Meza, E. R. Larios-Durán, A. Gutiérrez-Becerra, N. Casillas, J. I. Escalante and M. Bárcena-Soto, *J. Solid State Electrochem.*, 2019, **23**, 3123–3133.
53 T. Topală, A. Bodoki, L. Oprean and R. Oprean, *Clujul Med.*, 2014, **87**, 215.
54 Z. Zhu, Z. Wang, Y. Hao, C. Zhu, Y. Jiao, H. Chen, Y.-M. Wang, J. Yan, Z. Guo and X. Wang, *Chem. Sci.*, 2016, **7**, 2864–2869.
55 (*a*) L. D. Field, S. A. Walper, K. Susumu, G. Lasarte-Aragones, E. Oh, I. L. Medintz and J. B. Delehanty, *Bioconjugate Chem.*, 2018, **29**, 2455–2467; (*b*) D. Petrović, B. Stojimirović, B. Petrović, Z. M. Bugarčić and Ž. D. Bugarčić, *Bioorg. Med. Chem.*, 2007, **15**, 4203–4211; (*c*) J. Zajda, A. Wróblewska, L. Ruzik and M. Matczuk, *J. Controlled Release*, 2021, **335**, 178–190.
56 A. Setapa, N. Ahmad, S. M. Mahali and M. C. I. M. Amin, *Polymers*, 2020, **12**, 2921.
57 (*a*) X. Wang and Z. Guo, *Anti-Cancer Agents Med. Chem.*, 2007, **7**, 19–34; (*b*) B. J. Kim, T. W. Hambley and N. S. Bryce, *Chem. Sci.*, 2011, **2**, 2135–2142; (*c*) C. Y. Zeng, J. Ma, Y. Zhan, X. Xu, Q. Zeng, J. Liang and X. Chen, *Int. J. Nanomed.*, 2018, **13**, 6551–6574; (*d*) K. L. Ciesienski, L. M. Hyman, D. T. Yang, K. L. Haas, M. G. Dickens, R. J. Holbrook and K. J. Franz, *Eur. J. Inorg. Chem.*, 2010, 2224–2228; (*e*) J. Reedijk, *Chem. Rev.*, 1999, **99**, 2499–2510; (*f*) P. Zöllner, A. Zenker, M. S. Galanski, B. K. Keppler and W. Lindner, *J. Mass Spectrom.*, 2001, **36**, 742–753; (*g*) A. Reis, M. R. M. Domingues, P. Domingues, A. J. Ferrer-Correia and M. A. Coimbra, *Carbohydr. Res.*, 2003, **338**, 1497–1505; (*h*) S. Ahmad, *Polyhedron*, 2017, **138**, 109–124.
58 J. Liu, J. Johnson, J. Lu and M. J. McKeage, *Curr. Cancer Drug Targets*, 2012, **12**, 962–986.
59 C. F. Arias, F. J. Acosta, F. Bertocchini and C. Fernández-Arias, *Commun. Biol.*, 2025, **8**, 446.
60 I. Roy, K. T. Magesh, M. Sathyakumar, A. Sivachandran, D. Purushothaman and R. Aravindhan, *J. Pharm. BioAllied Sci.*, 2023, **15**, S630–S635.